ADVANCED ENERGY MATERIALS
www.advenergymat.de

Adaptive Multi-Site Gradient Adsorption of Siloxane-Based Protective Layers Enable High Performance Lithium-Metal Batteries

Shan Fang, Fanglin Wu, Shangquan Zhao, Maider Zarrabeitia, Guk-Tae Kim, Jae-Kwang Kim, Naigen Zhou, and Stefano Passerini**

Low Coulombic efficiency and significant capacity decay resulting from an unstable solid electrolyte interphase (SEI) and dendritic growth pose challenges to the practical application of lithium-metal batteries. In this study, a highly efficient protection layer induced by octaphenylsilsesquioxane (OPS) with LiFSI salt is investigated. The OPS exhibits a strong adsorption energy with lithium, its multi-site gradient adsorption ability enables the simultaneous capture of 8 Li^+ and the uniform regulation of Li ion flux. Moreover, the mechanical strength and electronic insulation of the OPS layer induces Li deposition under the protection layer and effectively inhibits lithium dendrite growth. Such a protection layer contributes to the stable and dendrite-free performance of a lithium-metal battery employing $LiNi_{0.8}Co_{0.1}Mn_{0.1}O_2$ (NCM811) as a cathode and an ultrathin OPS-protected lithium foil (20 µm) as the anode. A remarkable capacity retention of 91.4% is achieved after 300 cycles at 1C. The OPS-protected Li anodes and NCM811 are also tested in combination with a $Li_{1.5}Al_{0.5}Ge_{1.5}(PO_4)_3$ solid electrolyte, showing extended cyclability up to 300 cycles with an average Coulombic efficiency of 99.58% and capacity retention of 85.7%.

1. Introduction

Lithium metal with its ultrahigh specific energy (3860 mAh g^{-1}) and the lowest negative electrochemical potential (−3.04 V vs the H^+/H_2 redox couple) has gained wide research interest in recent years.[1] However, the high reactivity of lithium metal induces reaction with almost all electrolytes and the uncontrolled dendrite growth cause low Coulombic efficiency (CE) and fast capacity decay.[2] The solid electrolyte interphase (SEI) is a critical component of the lithium battery which is closely connected to the deposition morphology and electrochemical performance of lithium metal batteries (LMBs).[3] Researchers have determined that the SEI on lithium metal anode (LMA) must be homogeneous in composition, shape, and ionic conductivity, in addition to possessing the ability to conduct ions and block electrons.[4] Unfortunately, due to the use of conventional organic carbonate-based electrolyte, the inner layer of the SEI is dominated by more stable inorganic components, such as Li_2O, Li_2CO_3, and Li halides, whereas the outer layer is dominated by metastable organic compounds, such as ROCOOLi.[5,6] The SEI which comprises of the stacking of tiny domains with different composition has been described as the mosaic model,[7] which exhibits heterogeneous Li^+ conductivity

S. Fang, S. Zhao, N. Zhou
School of Physics and Materials
Nanchang University
Nanchang, Jiangxi 330031, P. R. China
E-mail: ngzhou@ncu.edu.cn

S. Fang, F. Wu, M. Zarrabeitia, G.-T. Kim, S. Passerini
Helmholtz Institute Ulm (HIU)
Helmholtzstrasse 11, 89081 Ulm, Germany
E-mail: stefano.passerini@kit.edu

S. Fang, F. Wu, M. Zarrabeitia, G.-T. Kim, S. Passerini
Karlsruhe Institute of Technology (KIT)
P.O. Box 3640, 76021 Karlsruhe, Germany

G.-T. Kim, J.-K. Kim
Department of Energy Convergence Engineering
Cheongju University
Cheongju, Chungbuk 28503, Republic of Korea

S. Passerini
Chemistry Department
Sapienza University of Rome
Piazzale a. Moro 5, Rome 00185, Italy

The ORCID identification number(s) for the author(s) of this article can be found under https://doi.org/10.1002/aenm.202302577

DOI: 10.1002/aenm.202302577

and results in inhomogeneous nucleation.[8] Additionally, the infinite volume expansion that occurs during cycling stimulates the creation of fissures in the SEI, exposing fresh Li to a lower energy barrier for Li-ion transport and exacerbating non-uniform deposition of Li.[9]

Although the use of hosts[10-13] and mechanically resistant films[14-16] can inhibit dendrite formation, the unstable SEI remains a major barrier for LMA materials. In recent years, great efforts have been devoted to improving the stability of the LMA interface. For instance, researchers have explored the use of high concentration electrolytes[17] and functional electrolyte additives[18-20] to regulate the constituents of SEI. However, the precise composition and structure of the SEI derived from electrolyte decomposition are diverse and uncontrolled, which is ineffective in inhibiting dendritic growth on the metallic Li anode. Therefore, the direct construction of an artificial protective layer has been proposed to promote uniform Li ion flux at the electrode/electrolyte interface[21-23] as well as to isolate lithium metal from direct contact with electrolyte, inhibiting side reactions and achieving a dendrite-free Li deposition anode.[24] One promising approach involves the use of a controlled Li diffusion interface based on lithiated multiwalled carbon nanotubes, which have been shown to effectively suppress dendrite formation. This is because the Li-C interface mediates Li^+ ion flux during the plating/stripping process, resulting in a more stable SEI and improved electrode/electrolyte interface.[25] Yan's group has designed a dual-layered film comprising a dense organic layer and rigid inorganic materials, mainly Li_3PO_4, which exhibits excellent mechanical properties and great flexibility.[26] Additionally, a modified Cu foil by an ultrathin thiophdiyne (TD) layer composed of thiophene units and acetylene bonds, could achieve a seaweed-like Li deposition morphology. The linked TD units with acetylene bonds can improve the extended conjugate structure, enhance the charge diffusion behavior and electro-negativity, leading to a strong binding energy between Li atoms and the lithiophilic TD substrate.[27,28] Consequently, the protective layer with lithiophilic structure is beneficial for guiding uniform Li nucleation and to alleviate dendrite formation.[29] However, a finite amount of lithiophilic site is provided on each molecule for most of the compounds. The presence of multiple lithiophilic sites on a single molecule can enhance the uniformity of lithium ions distributed on the electrode surface, prevent the aggregation and formation of uneven deposits, and promote the stability of the lithium anode.

Herein, an efficient strategy is proposed to regulate Li deposition behavior by introducing octaphenylsilsesquioxane (OPS) and incorporating a small amount of Li salt. The OPS demonstrates a high affinity for lithium, and its ability to adsorb lithium ions across multiple sites enables it to effectively capture and regulate the Li^+ ions flux homogenously. The protection layer homogenizes Li^+ flux and captures Li^+ on the surface, enabling dendrite-free lithium plating/stripping. Furthermore, the OPS layer acts as a physical barrier, preventing corrosion reactions between LMA and electrolyte. The addition of 1 wt.% of Li salt into the 25 mM OPS solution used as a Li inventory guarantees a stable electrode/electrolyte interface and facilitates electrochemical and mass transport kinetics in traditional carbonate-based electrolytes. The application of these protection layers to LMBs employing NCM811 has shown promising results. The protected lithium anode prolongs the lifetime of limited Li (20 μm) ||NCM811 cell to 300 cycles with a capacity retention of 91.4%, which is more than two times longer than the cell using bare lithium anode. Moreover, the artificial SEI enabled a high stability of the quasi-solid-state battery (LiOPS||LAGP||NCM811) with a high-capacity retention of 85.7% after 300 cycles.

2. Results and Discussion

The molecular structure of OPS is shown in Figure S1 (Supporting Information), the highest occupied molecular orbital (HOMO) and the lowest unoccupied molecular orbital (LUMO) energy levels of OPS are presented in **Figure 1a**. The calculated HOMO-LUMO gap of the OPS molecule is 4.65 eV, demonstrating a high electrochemical stability.[30] To create a protective layer on the surface of the lithium foil, a drop-casting method is employed (Figure 1b), as detailed in the Experimental section of the Supporting information. By varying the concentration of the OPS solution, the composition of the artificial SEI can be modulated to achieve optimal protection of the lithium electrode. The electrochemical kinetic stability of the Li foil treated with 25 mM OPS was determined to be the most stable at a high current density of 4 mA cm^{-2}, as depicted in Figure S2 (Supporting Information). This specific condition was selected for further in-depth analysis, and the protected Li was denoted as LiOPS. Scanning electron microscope (SEM) images of the LiOPS electrode (Figure 1c) demonstrates a smooth and matte texture surface in contrast to the bare Li foil (Figure S3, Supporting Information). X-ray photoelectron spectroscopy (XPS) was employed to validate the formation of the protecting layer on the surface of Li foil. Figure 1d–h shows the photoelectron spectra of Si 1s, O 1s, S 2p, N 1s, and Li 1s for the LiOPS electrode, indicating the successful coating of the protecting layer on the Li foil. Li 1s signal is very weak due to the thick OPS layer (≈200 nm, see the SEM image in Figure S4, Supporting Information). Furthermore, the presence of the OPS is confirmed by the O 1s, and Si 2p. The -Si-O-Si- bonding was evident in the O 1s (532.2 eV) and Si 2p (102 eV) regions. Moreover, S 2p and N 1s photoelectron spectra confirms the presence of LiFSI salt. The EDS analysis is consistent with the XPS data, as shown in Figure S5 (Supporting Information). The homogenous dispersion of the OPS layer is beneficial in establishing a uniform electric field and ion concentration, thereby facilitating the homogeneous Li^+ diffusion through the protecting layer.[22] In comparison, the surface composition of pure Li foil was also identified by XPS. In this case, the surface of Li foil is mainly composed of Li_2CO_3 and Li_2O (to a lesser extent), as shown in Figure S6 (Supporting Information).

The electrochemical kinetics at the electrode/electrolyte interface were evaluated by determining the exchange current density (J^0) of both Li foil and LiOPS using Tafel curves. The J^0 values were compared to assess the reversibility of the plating/stripping reactions, which is an important parameter for the study of the electrode kinetics. A higher J^0 value indicates a more efficient electrochemical reaction and a lower overpotential, which is essential for achieving uniform and stable Li deposition.[31] In Figure 1i, the J^0 values of LiOPS and bare Li foil are 1.977 and 1.027 mA cm^{-2}, respectively, indicating enhanced mass transfer and reduced surface diffusion barrier at the LiOPS anode. Galvanostatic electrodeposition tests were then performed with

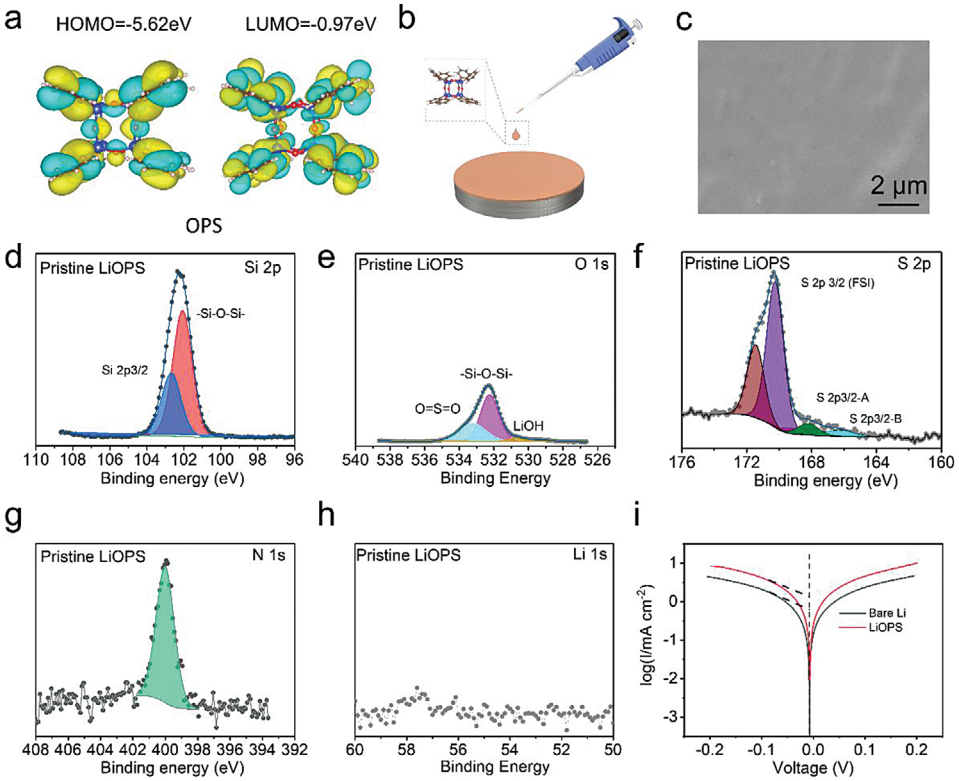

Figure 1. a) Calculated HOMO and LUMO energies according to the illustrated models. b) Schematic illustration of the fabrication process, c) SEM image of LiOPS, detailed XPS spectra of Si2p d), O1s e), S2p f), N1s g), Li1s h), and i) exchange current density of bare Li and LiOPS.

symmetric bare Li and LiOPS cells to investigate the impact of the functional protection layer on the interfacial stabilities of Li metal anode. **Figure 2** displays the plating/stripping behaviors of symmetric Li/Li and LiOPS/LiOPS cells at various current densities of 1, 2, 4 mA cm^{-2}, while the deposition capacity was fixed at 1 mAh cm^{-2}. The bare Li cell displayed a slight decrease in overpotential after initial stable cycling for ≈100 h, however, a rapid increase in polarization voltage was observed after ≈200 h (Figure 2a,b), exceeding 500 mV after 300 h at 1 mA cm^{-2}. Figure 2c provides the average plating and striping voltage, which offers a more comprehensive comparison between the two electrodes. The significant hysteresis observed indicates the formation of a highly resistive interfacial layer, primarily consisting of inactive Li and by-products of decomposed electrolyte. The sharp variation of voltage also suggests the uncontrolled dendrites self-propagation during the plating/stripping process. In contrast to the bare Li foil, the LiOPS cell demonstrates a consistent overpotential of ≈40 mV throughout the entire cycling process, lasting for 400 cycles (800 h), and displays flatter voltage profiles. As illustrated in Figure 2d,g, the stable plating/stripping voltage of LiOPS is observed even at higher current densities (2 mA cm^{-2} and 4 mA cm^{-2}). The corresponding overpotential was 170 and 240 mV (Figure 2f,i), respectively. However, significant fluctuation is detected in the symmetric cell with bare Li foil, which can be attributed to the growth of lithium dendrites and accumulation of "dead Li". Additionally, the LiOPS electrode exhibits excellent rate capability from 0.5 to 6 mA cm^{-2} with a constant capacity of 1 mAh cm^{-2} (Figure 2j). In comparison to bare Li foil, the LiOPS electrode demonstrates highly stable voltage oscillation and remarkably low overpotential at each current density, particularly at the high current density of 6.0 mA cm^{-2}, which suggests fast kinetic behavior for Li^+ transport. The thickness evolution of the electrode after the rate test was also analyzed by SEM (Figure S7, Supporting Information). The volume expansion of the bare Li foil is significant, resulting in the electrode thickness increasing by 106 μm (from 460 to 566 μm) after the rate test. On the other hand, the LiOPS electrode thickness increased by only 25 μm (460 to 485 μm), indicating that the Li deposition on the LiOPS electrode is more uniform and denser, enabling long-term plating/stripping cycling. The evolutions of interfacial resistance during cycling were monitored by electrochemical impedance spectroscopy (EIS), where all the Nyquist plots showed a full semicircle with a tail (Figure 2k,l). The diameter of the semicircle reflects the interfacial resistance between the electrolyte and the lithium metal electrode. Based on the results of the equivalent circuit fitting, the overall impedance of the cell is reduced significantly (from 268.8 to 91.4 Ω) by the protection layer prior to cycling (Figure 2m). The interfacial resistance of the LiOPS symmetric cell remains almost constant after plating/stripping at 1 mA cm^{-2} for 20 and 50 cycles, indicating a stable electrode/electrolyte interface that is consistent with the constant overpotential. However, the interfacial resistance of the bare Li symmetric cell continuously decreases during cycling, potentially due to the increased surface area resulting from lithium dendrite growth.[32] The results highlight the lower resistance of Li^+ diffusion through the OPS protection layer and the

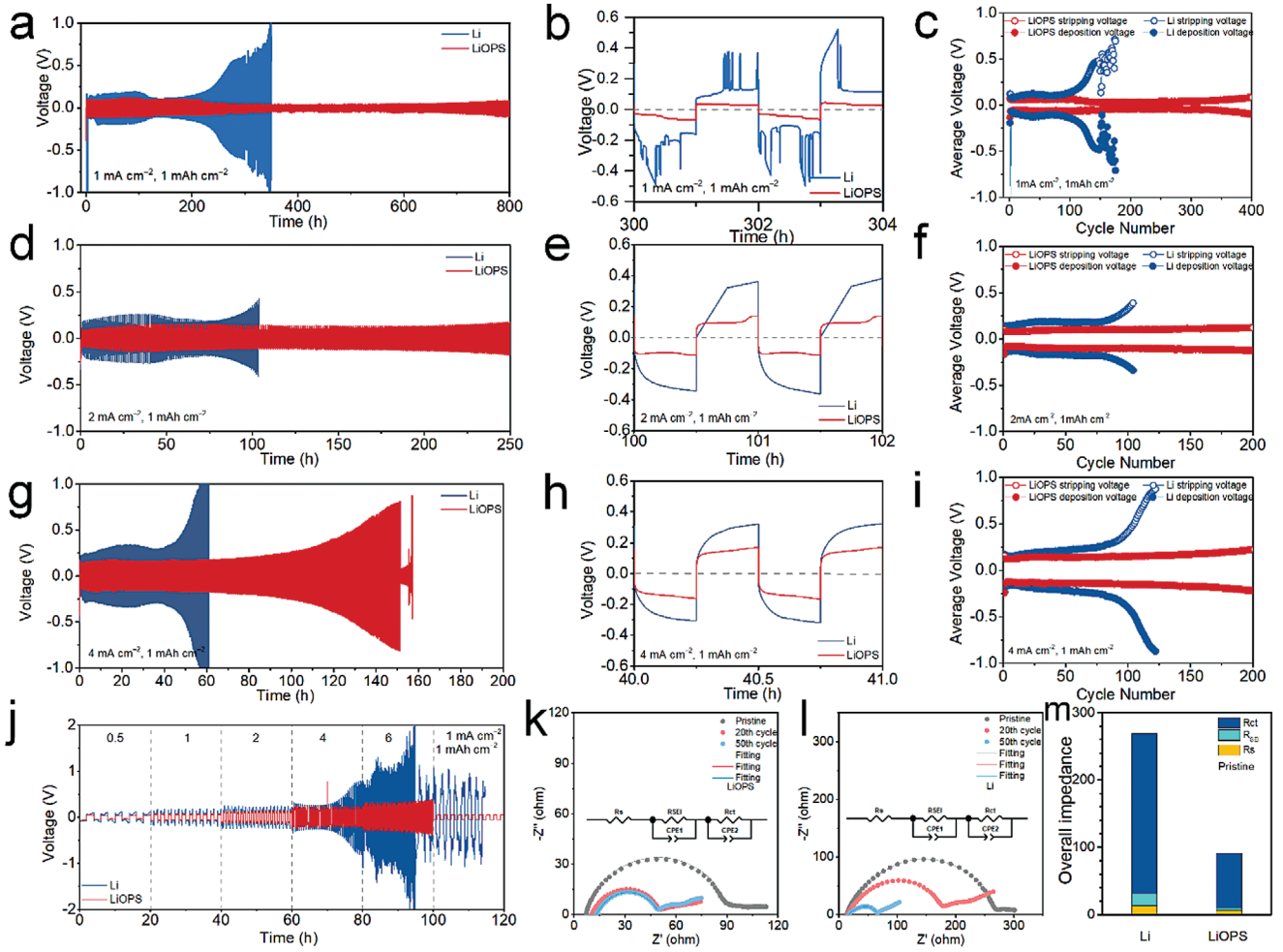

Figure 2. Performance of symmetric LiOPS (red) bare Li (blue) cells: a,d,g) plating/stripping behavior at different current densities (see legend) and b,e,h) magnified voltage profile as well as c,f,i) average voltage profiles calculated for each cycle. j) rate performance from 0.5 to 6 mA cm^{-2}, fixed deposition capacity of 1 mAh cm^{-2}. Electrochemical impedance spectra of the symmetric cell before and after cycles: k) LiOPS and l) bare Li impedance spectra upon cycling (including fitting lines) and m) overall impedance of LiOPS and bare Li cells before cycling.

mechanical strength of the interphase layer providing good mechanical stability to suppress the growth of Li dendrites during cycling.

To enhance the understanding of the lithium deposition mechanism, an in situ optical microscope monitoring was performed using a symmetric cell. The results revealed that the bare Li anode displayed an uneven surface after applying a current density of 0.5 mA cm^{-2} for 5 min, with large "mossy" clusters appearing on the surface and continuously growing over 30 min as the deposition capacity increased (**Figure 3a**, Video S1, Supporting Information). In contrast, a completely different phenomenon was observed with the LiOPS electrode, as shown in Figure 3b and Video S2 (Supporting Information). Throughout the whole process, no clusters were observed, indicating that the deposited Li was denser and more uniform on the electrode. SEM images presented in Figure 3c–h, Figures S8 and S9 (Supporting Information) display the lithium deposition morphology at various current densities. On the surface of the bare Li foil, nonuniform and uncontrolled growth of 1D lithium dendrites are evident (Figure 3f–h) even at a very low current density of 0.1 mA cm^{-2} (the uneven lithium deposition behavior on the bare Li electrode can be also observed in Figure S9c,d, Supporting Information). Conversely, highly dense and uniform lithium particles with several micrometers in width were observed on the LiOPS electrode at 1 mA cm^{-2}. Moreover, as the current density increased, smaller and denser lithium particles formed. Even at 4 mA cm^{-2}, no needle-like lithium formed. It is important to note that, besides the characteristics of the protective layer, the growth rate and morphology of Li can be strongly influenced by electrochemical test conditions, such as the charge current density. According to electrocrystallization nucleation theory, a higher current density leads to a higher overpotential and a greater number of lithium nuclei, resulting in smaller nucleation size.[33] These results demonstrate the superiority of the modified Li anode in obtaining good interfacial ion distribution at high current densities and avoiding the growth of Li dendrites. The hybrid layer can redistribute the Li^+ flux and provide rapid Li^+ transport simultaneously, in addition to acting as a physical barrier to protect lithium from corrosion of the electrolyte.

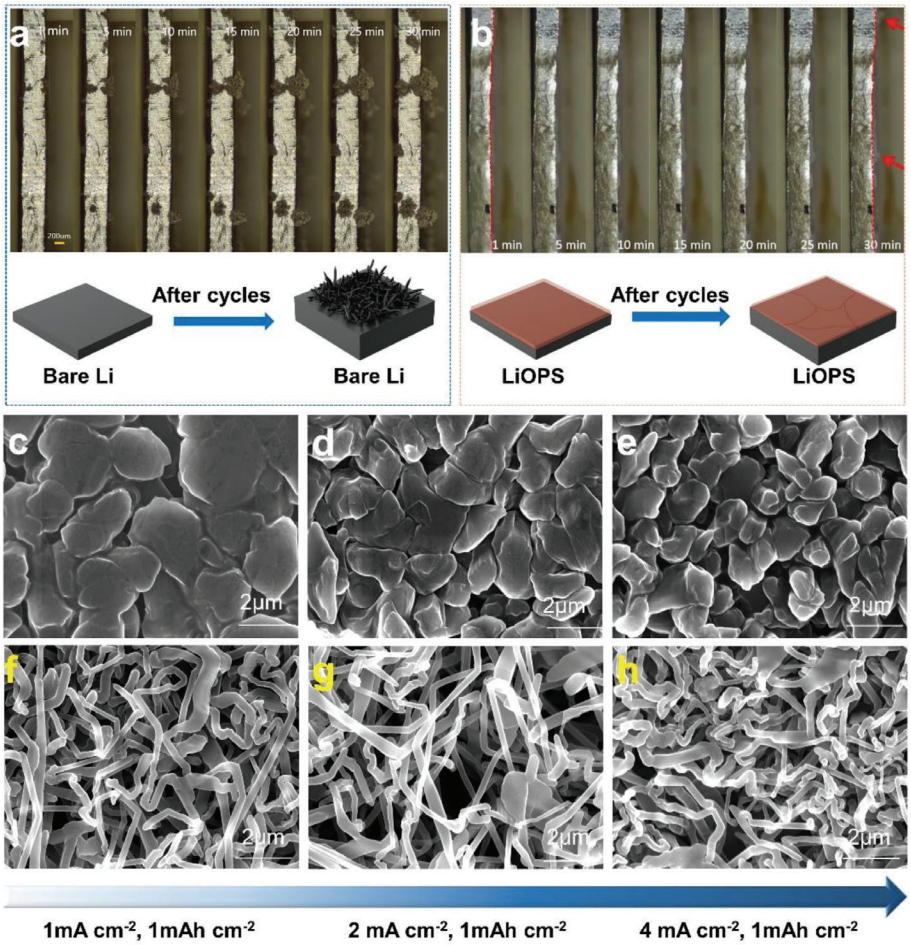

Figure 3. Optical images of bare Li a) and LiOPS b) taken at different times and corresponding schematic diagrams. SEM images of LiOPS c,d,e) and bare Li f,g,h) electrodes after the first deposition at different current densities, but constant deposition capacity (see figure legend).

Bare Li and LiOPS symmetric cells were cycled and the XPS spectra were collected after 10 cycles at 1 mA cm^{-2}, 1mAh cm^{-2} (**Figure 4**a,b). A higher intensity of LiF (F 1s, 684.9 eV), Li_2CO_3 (O1s, 531.7 eV), and Li_2O (O1s, 527.9 eV) was detected in the SEI layer of LiOPS cell, hence is composed by a higher ratio of inorganic components. While the SEI layer of bare Li shows higher content ratio of -C-C/-CH- (hydrocarbons), and $Li_xPF_y/Li_xPF_yO_z$ than those of LiOPS. Therefore, these results demonstrate that the OPS coating layer suppressed the electrolyte decomposition and formed a highly dense inorganic-rich SEI layer. The higher proportion of inorganic components can improve the ionic conductivity of the SEI layer of LiOPS and homogenizes Li ion flux, thus prohibiting lithium dendrite formation during Li plating and stripping.

To systematically evaluate the load behavior of Li atoms after the OPS adsorbed on the Li (110) anode surface, we have calculated possible sites for Li atoms around the OPS. As shown in Figure 4c, namely the vertical position of the benzene ring center (D1, M1, and U1), symmetrical positions corresponding to the body center (M4), face center (D2, M2, and U2) and edge center (D3, M3, and U3) of the cage composed of Si—O bonds. For comparison, the adsorption energy of Li atoms was also calculated excluding the influence of the OPS (R0 site), which indicates the adsorption energy of Li atoms on Li foil. Based on the calculation results, Figure 4d illustrates ten possible adsorption sites for Li and their respective formation energies. It is evident that the adsorption of OPS on lithium atoms demonstrates a gradient effect in terms of energy adsorption.

It is worth noting that when Li ions are loaded on the center of two benzene rings (i.e., D sites), the two benzene rings will rotate towards the Li ions, which will lead to significant structural changes in OPS and thereby affecting the adsorption energy at other locations. Besides, Li atoms located at the D2 position are metastable, and once D3 positions are occupied, the Li atoms at D2 position will transfer to either D1 or D3 positions, demonstrate smart and self-adaptive properties. Additionally, D1 and D3 sites exhibit higher affinity for Li ion adsorption compared to the bare Li surface (i.e., R0 sites). The charge density deformation diagram for an OPS molecule adsorbing four and eight Li atoms is depicted in Figure 4e,f. It is observed that the number of Li atoms adsorbed between OPS and Li anode increase, the interaction between OPS and Li anode is enhanced, leading to the deformation of the Si-O cage within the OPS molecule. The lithium deposition mechanism on Li anode, with and without OPS protection layer, is illustrated in Figure 4g–j. In the case of bare Li foil, the nonuniform Li ion flux and heterogeneous SEI layer cause preferential

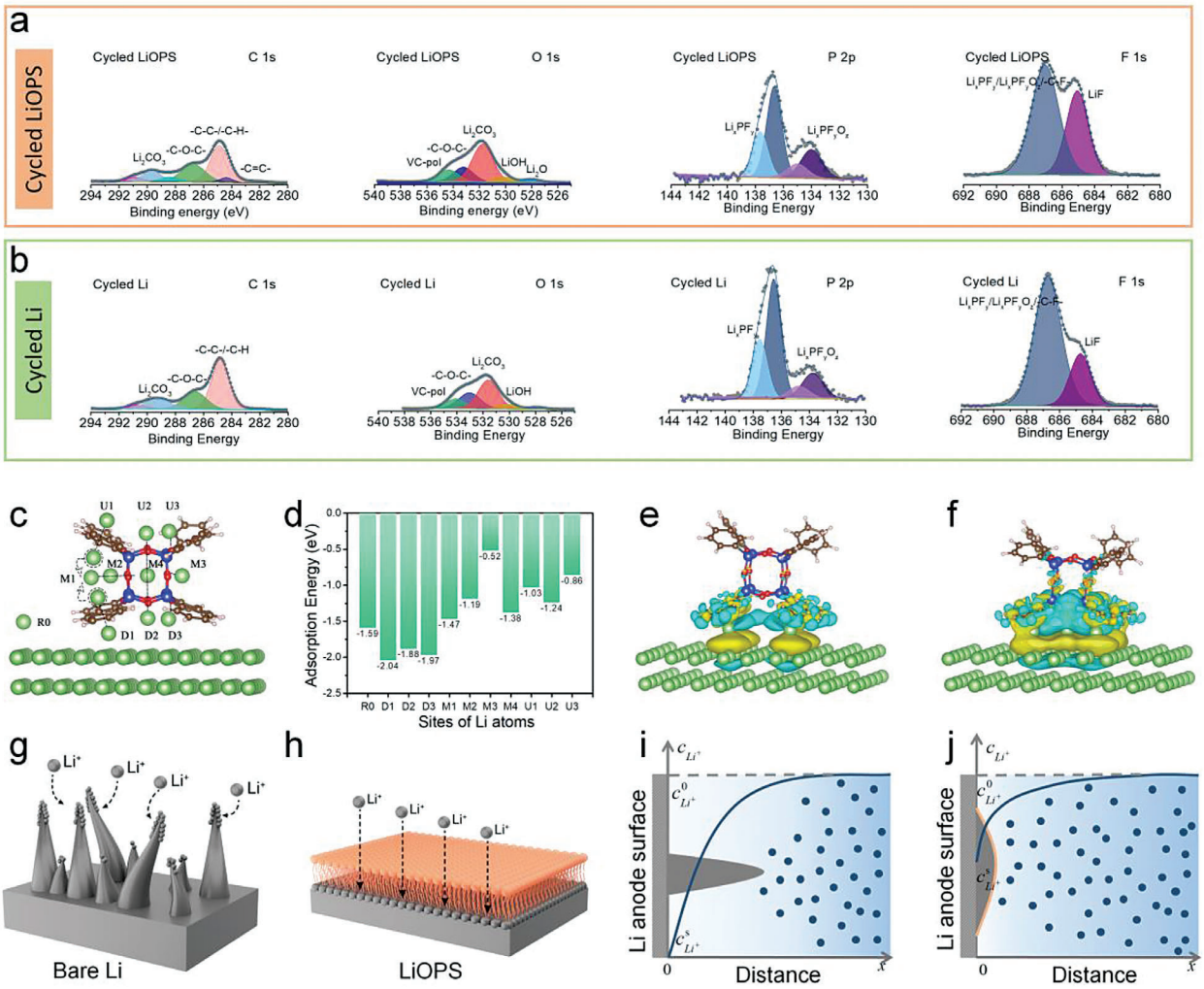

Figure 4. Detailed XPS spectra of cycled LiOPS a) and bare Li b), c) available Li adsorption sites around OPS and d) their adsorption energy. Differential charge density diagram when OPS adsorbs 4 (D1 position) e) and 8 (D1 and D3 positions) Li atoms f), respectively. The schematic of the Li plating process with and without OPS g,h). i,j) display the concentration gradients of Li^+ and the corresponding Li deposition morphologies. $c^0_{Li^+}$ $c^0_{Li^+}$ is the electrolyte concentration, $c^0_{Li^+}c^s_{Li^+}$ is the concentration of the liquid layer near the electrode surface.

deposition of Li ions on hotspots, resulting in the formation of protrusions.[34] The high curvature of these protrusions generates a stronger electric field at their tips, attracting more Li-ions and accelerating the evolution of a strong concentration gradient of Li ion, leading to further growth of the protrusions and ultimately resulting in dendrite formation (Figure 4i).[35–37] On the contrary, the presence of the OPS protection layer with varying Li ion adsorption capabilities in 3D space promotes more uniform Li ion flux. The Li is deposited in bulk particles instead of needle-like morphologies, which inhibits the formation of a strong concentration gradient (Figure 4j). Consequently, this improves the reversibility of Li during plating/stripping process and reduces dead Li formation.[38]

Lithium metal full cells assembled with a 450 µm Li anode and NCM811 cathode (areal loading: 9.1 mg cm^{-2}) has been investigated. The initial discharge capacity was 159.6 mAh g^{-1} at 1 C for both cells (see **Figure 5**a). After 300 cycles, however, the discharge capacity of LiOPS||NCM811 cell is 136.3 mAh g^{-1}, which corresponds to a capacity retention of 85.4%. In contrast, the bare Li full cell only offers 87.5 mAh g^{-1} with a capacity retention of 53.7% (Figure 5a). This significant difference indicates that severe capacity decay occurred in the Li||NCM811 cell, as is evident in the charge/discharge curve displayed in Figure S10 (Supporting Information). The polarization of the Li||NCM811 cell is observed to be significant, which is mainly due to the uncontrolled growth of dendrites and dead lithium during the long-term cycling, leading to an increase in the internal resistance of the cell. However, the polarization is much lower in the LiOPS||NCM811 cell as shown in Figure 5b. Moreover, the high-frequency part of the LiOPS||NCM811 cell impedance spectra before and after selected cycles is almost overlapping, indicating an enhanced stability in the electrode/electrolyte interface with respect to those of the Li||NCM811cell (Figure S11, Supporting Information). To evaluate practical application, a thin lithium foil with a thickness of 20 µm (≈4 mAh cm^{-2}) has been used as a replacement for the thick lithium, which provides a realistic performance of

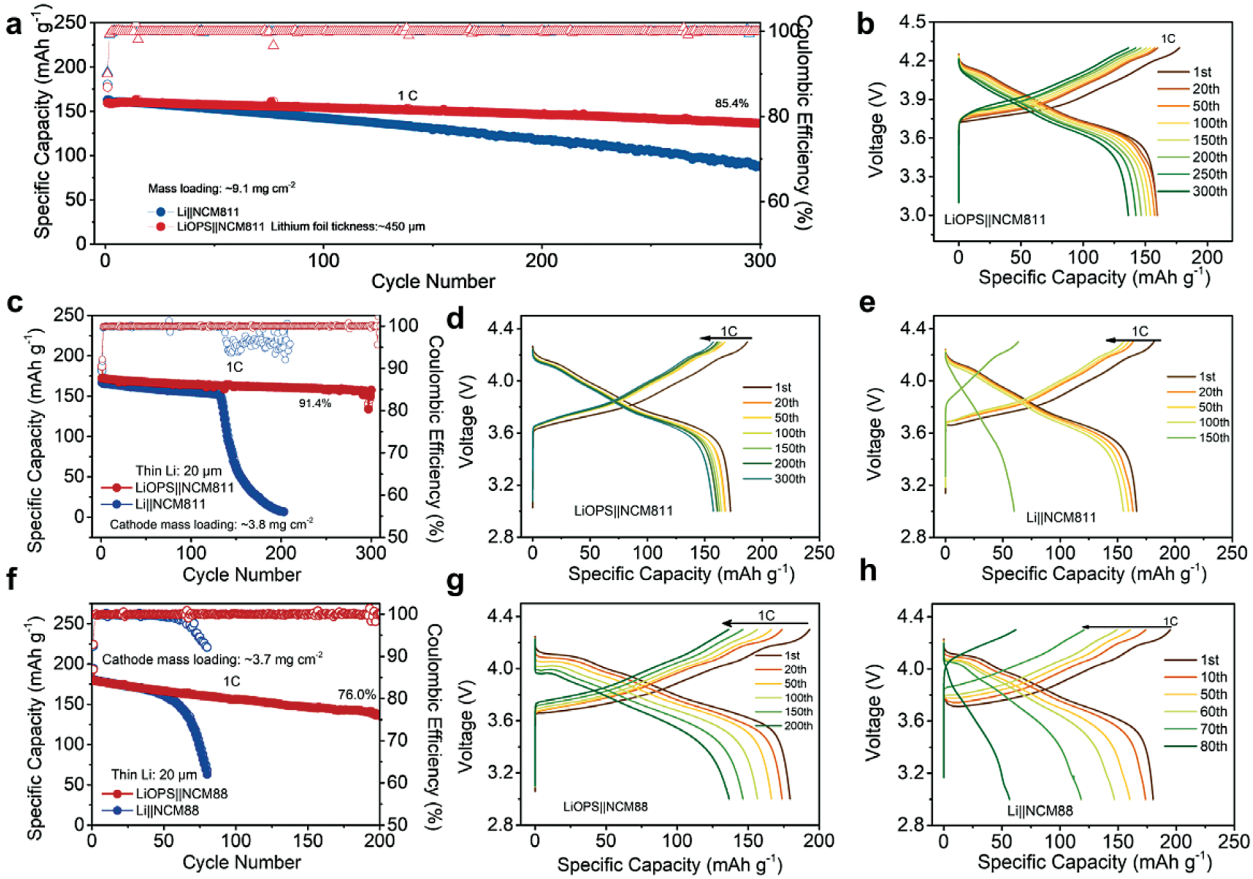

Figure 5. Electrochemical performance comparison of bare Li and LiOPS with high nickel content NCM811 a–e) and NCM88 f–h) cathodes. (a) Long term cycling of bare Li and LiOPS with an unlimited lithium foil (thickness: 450 μm) at a high areal loading of ≈9.1 mg cm^{-2} and (b) selected voltage profiles for LiOPS, (c) comparison of cycling behavior of bare Li and LiOPS with NCM811 using a thin lithium foil (thickness: 20 μm), corresponding voltage curves of (d) LiOPS and (e) bare Li, (f) comparison of cycling behavior of bare Li and LiOPS with NCM88 using a thin lithium foil (thickness: 20 μm) and selected voltage profiles for (g) LiOPS and (h) bare Li.

the Li-metal battery. As shown in Figure 5c, after the first five formation cycles at 0.1C (1C = 200 mA g^{-1}), the cells cycled at 1C for the following cycles at the voltage range of 3.0–4.3 V. The LiOPS||NCM811 cell demonstrated excellent cycling stability, maintaining a high discharge capacity of 157.5 mAh g^{-1} even after 300 cycles. The corresponding capacity retention rate was exceptionally high at 91.4%, and the average CE was also impressively high at 99.94%. The Li||NCM811 cell experiences a rapid decrease in capacity after the 135th cycle, in contrast to the LiOPS||NCM811 cell. This is due to the formation of dendritic Li, accelerating the reaction between fresh Li and electrolyte to form SEI. As the cycling proceeded, metallic Li is trapped by the insulating SEI and lose electron connection, thus becoming "dead Li".[38-40] When the active Li has been depleted, the cell experiences fast capacity decay and a short cycle life. Figure 5d depicts the selected charge/discharge curves, the shoulder of the charge curve demonstrates the start of delithiation in NCM811, which corresponds to Li deposition on the anode side.[41] By virtue of the effective protection layer of OPS homogenized Li^+ flux, negligible voltage polarization is observed, indicating low ionic migration barrier for Li nucleation and plating. However, Figure 5e shows a drastic increase of electrode polarization at the 150th when assembled with bare Li. The high repeatability of the cell performance tests is shown in Figure S12 (Supporting Information). Then, the full cell assembled with a high areal loading cathode (9.2 mg cm^{-2}) and thin Li foil (20 μm), corresponding to a low N/P ratio of 2.17, was also evaluated (see Figure S13, Supporting Information). The first charge/discharge capacity was 188.1/168.4 mAh g^{-1}. After 70 cycles at 1 C, the discharge capacity is 135.7 mAh g^{-1}, corresponding to a capacity retention of 80.6%. To further improve the specific capacity of lithium metal battery, the electrochemical performance was investigated by employing a higher nickel content of $LiNi_{0.88}Co_{0.09}Mn_{0.03}O_2$ (NCM88). The thin LiOPS||NCM88 cell delivered an impressive charge/discharge capacity of 230.8/208.0 mAh g^{-1} for the first cycle at 0.1 C (Figure S14, Supporting Information). The cell displayed a discharge capacity of 136 mAh g^{-1} at 1 C with a capacity retention of 76.0% after 200 cycles. In contrast, the thin Li||NCM88 exhibited an inferior cycling performance, with a drastic capacity decay even after 60 cycles, coinciding with an increase in voltage hysteresis. The electrochemical performance of the Li metal battery coupled with NCM88 cathode is found to be inferior compared to the cell matched with NCM811 cathode. This is because high nickel content cathode are more prone to

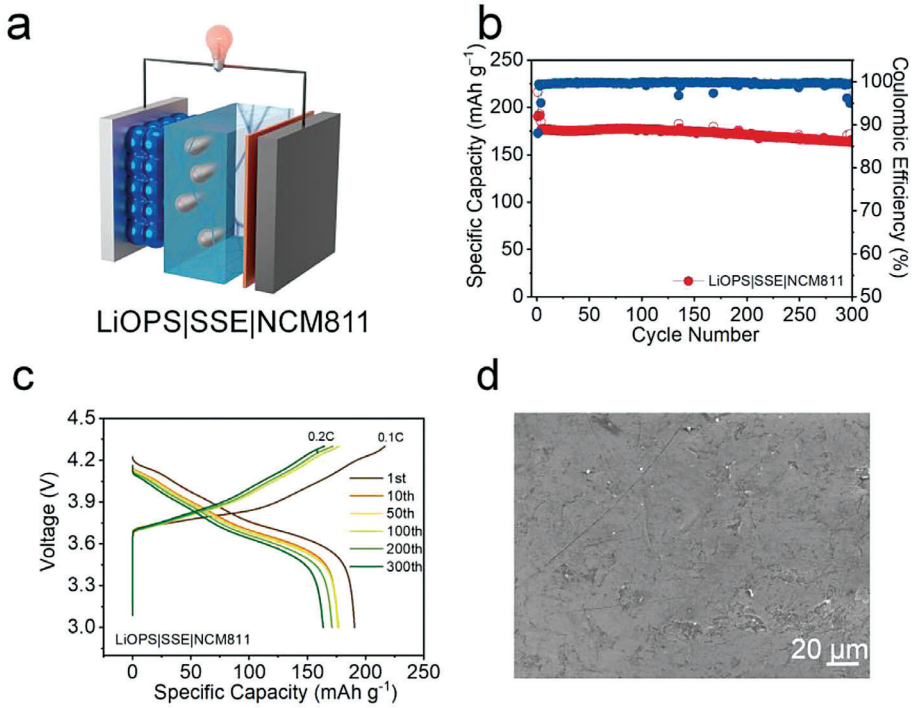

Figure 6. Schematic diagram of the solid-state cell a) and corresponding cycling behavior b,c), as well as the morphology of the cycled LiOPS electrode d).

microcracking due to volume changes caused by H2-H3 phase transitions, allowing the electrolyte to penetrate inside, causing an increase in impedance and a rapid capacity decay.[42] This is the main reason for the difference in cycling performance observed with the LiOPS anode.

Solid-state batteries, employing lithium metal as the anode, are regarded as a prospective alternative to conventional lithium-ion batteries due to their safety and potential for achieving higher energy densities. However, their practical implementation has been impeded by the instability of the interface between lithium metal electrodes and solid-state electrolytes (SSE), as well as the high solid-solid contact resistance.[43-45] To overcome these challenges, the use of OPS as a protective layer between the Li anode and solid electrolyte has been explored, with the aim of improving the electrochemical stability and contact between the two components. A solid-state battery was assembled using $Li_{1.5}Al_{0.5}Ge_{1.5}(PO_4)_3$ (LAGP) as the electrolyte, and NCM811 was utilized as the cathode to investigate the effectiveness of the LiOPS anode. It should be mentioned that 40 μL carbonate-based electrolyte was added on the surface of cathode as a wetting agent to improve interfacial contact between electrode and solid electrolyte without compromising safety. As shown in **Figure 6**, the cell delivers a discharge capacity of 216.3/190.5 mAh g^{-1} with an initial CE of 88.1%. After the first three formation cycles at 0.1 C, the cell displays high stability with a capacity retention of 85.7% after 300 cycles at 0.2 C, accompanied by an average CE of 99.58%. Subsequently, the cell was dissembled for SEM characterization. As shown in Figure 6d, some holes have been observed on the surface of LiOPS but no dendrites were formed. The results indicate that the OPS layer effectively improves the stability of the lithium metal-solid electrolyte interface and prevents lithium metal corrosion.

3. Conclusion

To summarize, a protective layer with a propensity to capture Li^+ and homogenize Li ion flux was designed and investigated. The OPS layer demonstrated superior performance in regulating homogeneous Li plating/stripping and improving electrochemical performance by facilitating the redistribution of Li^+ ions through multi-site adsorption. Furthermore, the protective layer demonstrated self-adaptive properties that prevented self-destruction by adjusting the adsorption sites when the amount of absorbed lithium exceeded eight atoms. The protected Li metal anode exhibited improved electrochemical performance in various cell configurations, including stable cycling performance for 300 cycles with high-capacity retention in the thin Li-OPS||NCM811 full cell and good stability for long-term cycles in the LiOPS||SSE||NCM811 cell. These strategies for constructing OPS layers using a simple drop-casting method provide a framework for the development of dendrite-free lithium metal anodes and promote the practical application of lithium metal batteries.

Supporting Information

Supporting Information is available from the Wiley Online Library or from the author.

Acknowledgements

Project funded by the National Natural Science Foundation of China (52002176, 52161039, 52062035), Jiangxi Provincial Natural Science

Foundation (20212BAB214054, 20224BAB204011) and the Helmholtz Association, the Industrial Cluster Program through Korea Industrial Complex Corporation (1415181452).

Open access funding enabled and organized by Projekt DEAL.

Conflict of Interest

The authors declare no conflict of interest.

Author Contributions

S.F. and F.W. contributed equally to this work. S.F. designed the experiment, performed the characterization and electrochemical measurements, data analysis, and wrote the manuscript. F.W. performed the electrochemical measurements, the preparation of LAGP solid electrolyte and revised the manuscript. S.Z. performed the DFT calculation, data analysis. M.Z. performed the XPS measurements and revised the manuscript. G.-T.K. discussed the experimental work and revised the manuscript. J.-K.K. provided NCM811 cathode material. N.G.Z. performed the DFT calculation, data analysis and revised the manuscript. S.P. conceptualized and coordinated the activities, provided funding for the work, and revised the manuscript.

Data Availability Statement

The data that support the findings of this study are available on request from the corresponding author. The data are not publicly available due to privacy or ethical restrictions.

Keywords

dendrite-free lithium anodes, lithium metal batteries, Ni-rich cathodes, protective layers, siloxane

Received: August 7, 2023
Revised: October 3, 2023
Published online:

[1] X. Zeng, M. Li, D. Abd El-Hady, W. Alshitari, A. S. Al-Bogami, J. Lu, K. Amine, *Adv. Energy Mater.* **2019**, *9*, 1900161.
[2] X. B. Cheng, R. Zhang, C. Z. Zhao, Q. Zhang, *Chem. Rev.* **2017**, *117*, 10403.
[3] Q. Zhao, S. Stalin, L. A. Archer, *Joule* **2021**, *5*, 1119.
[4] E. Peled, S. Menkin, *J. Electrochem. Soc.* **2017**, *164*, A1703.
[5] S. Chattopadhyay, A. L. Lipson, H. J. Karmel, J. D. Emery, T. T. Fister, P. A. Fenter, M. C. Hersam, M. J. Bedzyk, *Chem. Mater.* **2012**, *24*, 3038.
[6] Y. Ein-Eli, D. Aurbach, A. Zaban, *J. Electrochem. Soc.* **1994**, *141*, L1.
[7] E. Peled, D. Golodnitsky, G. Ardel, *J. Electrochem. Soc.* **1997**, *144*, L208.
[8] W. Liu, P. Liu, D. Mitlin, *Adv. Energy Mater.* **2020**, *10*, 2002297.
[9] Y. C. Yaron, S. Cohen, D. Aurbach, *J. Phys. Chem. B* **2000**, *104*, 12282.
[10] D. Y. K. Sungjin Cho, J.-I. Lee, J. Kang, H. Lee, G. Kim, D.-H. Seo, S. Park, *Adv Funct. Mater.* **2022**, *32*, 2208629.
[11] Y. Ren, W. Shin, A. Manthiram, *Adv. Energy Mater.* **2022**, *12*, 2200190.
[12] H. Chen, A. Pei, J. Wan, D. Lin, R. Vilá, H. Wang, D. Mackanic, H.-G. Steinrück, W. Huang, Y. Li, A. Yang, J. Xie, Y. Wu, H. Wang, Y. Cui, *Joule* **2020**, *4*, 938.
[13] S. Fang, L. Shen, A. Hoefling, Y. Wang, G. Kim, P. A. van Aken, X. Zhang, S. Passerini, *Nano Energy* **2021**, *89*, 106421.
[14] Y. Gao, T. Rojas, K. Wang, S. Liu, D. Wang, T. Chen, H. Wang, A. T. Ngo, D. Wang, *Nat. Energy* **2020**, *5*, 534.
[15] Z. Wang, Y. Wang, Z. Zhang, X. Chen, W. Lie, Y. B. He, Z. Zhou, G. Xia, Z. Guo, *Adv. Funct. Mater.* **2020**, *30*, 2002414.
[16] C. Chang, Y. Yao, R. Li, Z. H. Guo, L. Li, C. Pan, W. Hu, X. Pu, *Nano Energy* **2022**, *93*, 106871.
[17] N. Sun, R. Li, Y. Zhao, H. Zhang, J. Chen, J. Xu, Z. Li, X. Fan, X. Yao, Z. Peng, *Adv. Energy Mater.* **2022**, *12*, 2200621.
[18] C. Yan, X.-B. Cheng, Y. Tian, X. Chen, X.-Q. Zhang, W.-J. Li, J.-Q. Huang, Q. Zhang, *Adv. Mater.* **2018**, *30*, 1707629.
[19] Z. Yu, H. Wang, X. Kong, W. Huang, Y. Tsao, D. G. Mackanic, K. Wang, X. Wang, W. Huang, S. Choudhury, Y. Zheng, C. V. Amanchukwu, S. T. Hung, Y. Ma, E. G. Lomeli, J. Qin, Y. Cui, Z. Bao, *Nat. Energy* **2020**, *5*, 526.
[20] S. Fang, Y. Zhang, X. Liu, *Chem. Eng. J.* **2021**, *426*, 131880.
[21] S. Gao, Y. Pan, B. Li, M. A. Rahman, M. Tian, H. Yang, P.-F. Cao, *Adv. Funct. Mater.* **2022**, *33*, 2210543.
[22] A. Hu, W. Chen, X. Du, Y. Hu, T. Lei, H. Wang, L. Xue, Y. Li, H. Sun, Y. Yan, J. Long, C. Shu, J. Zhu, B. Li, X. Wang, J. Xiong, *Energ Environ. Sci.* **2021**, *14*, 4115.
[23] J. Zeng, Q. Liu, D. Jia, R. Liu, S. Liu, B. Zheng, Y. Zhu, R. Fu, D. Wu, *Energy Storage Mater.* **2021**, *41*, 697.
[24] S.-Y. Lee, J. Shangguan, J. Alvarado, S. Betzler, S. J. Harris, M. M. Doeff, H. Zheng, *Energ Environ. Sci.* **2020**, *13*, 1832.
[25] R. V. Salvatierra, G. A. Lopez-Silva, A. S. Jalilov, J. Yoon, G. Wu, A. L. Tsai, J. M. Tour, *Adv. Mater.* **2018**, *30*, 1803869.
[26] X. Liu, J. Liu, T. Qian, H. Chen, C. Yan, *Adv. Mater.* **2019**, *32*, 1902724.
[27] K. Wang, X. Li, J. Gao, Q. Sun, Z. Yang, J. He, S. Cui, C. Huang, *Adv. Funct. Mater.* **2021**, *31*, 2009917.
[28] K. Park, J. B. Goodenough, *Adv. Energy Mater.* **2017**, *7*, 1700732.
[29] C. X. Chen, X-.R. Chen, T.-Z. Hou, B.-Q. Li, X.-B. Cheng, R. Zhang, Q. Zhang, *Sci. Adv.* **2019**, *5*, 7728.
[30] R. G. Pearson, *J. Org. Chem.* **1989**, *54*, 1423.
[31] Z. Ju, C. Jin, X. Cai, O. Sheng, J. Wang, J. Luo, H. Yuan, G. Lu, X. Tao, Z. Liang, *ACS Energy Lett.* **2023**, *8*, 486.
[32] S. Li, Q. Liu, J. Zhou, T. Pan, L. Gao, W. Zhang, L. Fan, Y. Lu, *Adv. Funct. Mater.* **2019**, *29*, 1808847.
[33] E. Budevski, G. Staikov, W. J. Lorenz, *Electrochim. Acta* **2000**, *45*, 2559.
[34] Y. Zhang, T.-T. Zuo, J. Popovic, K. Lim, Y.-X. Yin, J. Maier, Y.-G. Guo, *Mater. Today* **2020**, *33*, 56.
[35] X. Jie, *Science* **2019**, *366*, 426.
[36] F. Ding, W. Xu, G. L. Graff, J. Zhang, M. L. Sushko, X. Chen, Y. Shao, M. H. Engelhard, Z. Nie, J. Xiao, X. Liu, P. V. Sushko, J. Liu, J.-G. Zhang, *J. Am. Chem. Soc.* **2013**, *135*, 4450;
[37] D. Lin, Y. Liu, Y. Cui, *Nat. Nanotechnol.* **2017**, *12*, 194.
[38] C. Fang, X. Wang, Y. S. Meng, *Trends Chem.* **2019**, *1*, 152.
[39] S. Chen, J. Zheng, D. Mei, K. S. Han, M. H. Engelhard, W. Zhao, W. Xu, J. Liu, J.-G. Zhang, *Adv. Mater.* **2018**, *30*, 1706102;
[40] C. Fang, J. Li, M. Zhang, Y. Zhang, F. Yang, J. Z. Lee, M.-H. Lee, J. Alvarado, M. A. Schroeder, Y. Yang, B. Lu, N. Williams, M. Ceja, L. Yang, M. Cai, J. Gu, K. Xu, X. Wang, Y. S. Meng, *Nature* **2019**, *572*, 511.
[41] B. D. Adams, J. Zheng, X. Ren, W. Xu, J.-G. Zhang, *Adv. Energy Mater.* **2018**, *8*, 1702097.
[42] F. Wu, S. Fang, M. Kuenzel, A. Mullaliu, J.-K. Kim, X. Gao, T. Diemant, G.-T. Kim, S. Passerini, *Joule* **2021**, *5*, 2177.
[43] K. J. Kim, M. Balaish, M. Wadaguchi, L. Kong, J. L. M. Rupp, *Adv. Energy Mater.* **2020**, *11*, 2002689.
[44] R. Zhao, L. Gao, M. Song, Y. Ye, Z. Liang, J. Bian, J. Zhu, S. Li, R. Zou, Y. Zhao, *ACS Energy Lett.* **2021**, *6*, 3141.
[45] X. Yang, X. Gao, S. Mukherjee, K. Doyle-Davis, J. Fu, W. Li, Q. Sun, F. Zhao, M. Jiang, Y. Hu, H. Huang, L. Zhang, S. Lu, R. Li, T. K. Sham, C. V. Singh, X. Sun, *Adv. Energy Mater* **2020**, *10*, 2001191.